ID 146

Investigation of Dynamic Stall Control by Deployable Vortex Generator using Time-Resolved PIV Analysis and URANS Computations

G. Joubert, A. Le Pape
ONERA-The French Aerospace Lab, 92190 Meudon, France

B. Heine
DLR, 37073 Göttingen, Germany

S. Huberson
Université de Poitiers, SFA-LEA, 86962 Futuroscope, France

Abstract

The flow over an OA209 airfoil subjected to a sinusoidal pitching motion under dynamic stall conditions and equipped with an innovative Deployable Vortex Generator actuator for stall control was experimentally and numerically investigated. Pressure and PIV measurements allow a comparison to be performed between clean and controlled cases. Separation point detection and Proper Orthogonal Decomposition are included in the analysis. Along with wind tunnel testing, numerical simulations were performed by solving the Unsteady RANS equations with the ONERA elsA code. Computations are sucessfully compared to the experimental reference and bring further understanding of the Deployable Vortex Generator actuation.

Introduction

Dynamic stall is an aerodynamically highly complex phenomenon occurring on helicopter main rotor blades during high-speed forward flight and certain maneuvers. During these flight conditions, the blade angle of attack may reach very high values on the retreating side of the rotor cycle. Combined with low relative velocities on the retreating blade, this can lead to massive unsteady flow separation. Depending on the airfoil characteristics, such an aerodynamic event can produce a temporary increase in drag, lift and especially strong negative pitching-moment peaks[12]. Structural damage may occur on the rotor commands due to these excessive loads. The dynamic stall therefore limits the high speed and maneuver flight capabilities of helicopters. Alleviating dynamic stall has been the subject of numerous studies; the most effective control methods, such as leading-edge slat[11] or airfoil drooping leading edge[2] have not yet come to aircraft application, because of difficulties to be applied on real helicopter blades. More recently, the use of the classical "vortex generator" (VG) actuator has been tested for dynamic stall control: contra-rotative VGs over the airfoil upper side[10] and so-called LeVOGs[9],[6].

A new concept of dynamic stall control actuators has recently been designed and tested in the ONERA F2 wind-tunnel facility[8]. The actuator consists in a row of co-rotative deployable vortex generators (DVGs) located at the leading-edge of the airfoil.

The present work aims at understanding the DVG control effect over dynamic stall. This was achieved on one hand with experimental data resulting from wind-tunnel testing including time-resolved Particle Image Velocimetry (PIV) analysis, and on the other hand through numerical simulations using 2D and 3D URANS models. For these calculations, the results of our previous work was used[7], especially in order to set the numerical parameters and grids size.

1 Airfoil and flow case

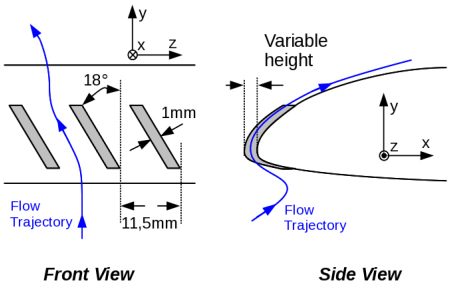

Figure 1: Sketch of the OA209 Airfoil nose showing Vortex Generators extruded from the leading edge.

The present study applies the strong correlation between real rotor blade motion and 2D airfoil oscillation that has been established[12] and widely used in the past decades. The present work focuses on the DVG

control effect over a pitch-oscillating 2D airfoil.

The flow conditions are set to a dynamic stall test case, with a chord-based Reynolds number $Re = 1.8 \times 10^6$ and a Mach number $M = 0.16$. The half-chord based reduced frequency is set to $k = 0.1$. The mean angle of attack is 13° and the oscillation amplitude is 5°. These parameters correspond to representative real-helicopter blade flight conditions[5]. Experimental and numerical investigations are performed on the rotor blade airfoil OA209[20], modified through addition of a co-rotative deployable vortex generators (DVG) row. The DVG consists of a 1.0 mm thick flat blade extruded from the leading-edge surface in the forward direction. It leans by 18° from the vertical reference. Spacing between two consecutive VG in the spanwise direction is equal to 11.5 mm (Fig. 1). The DVGs are deployable, i.e. their height h can be controlled. For a non-zero height the DVGs induce longitudinal vortices above the airfoil. The wind-tunnel testing showed that the DVG height of 1.5 mm was optimal for the Dynamic Stall control efficiency[8]. In the present paper, all result corresponds to this fixed-height DVG configuration.

2 Experimental results

The wind tunnel experiments of dynamic stall control using DVGs took place in the framework of the ONERA-DLR SIMCOS joint project. Lift and moment coefficients were measured through unsteady pressure sensors integration. Time-resolved Particle Image Velocimetry (tPIV) measurements were also conducted in the cross sectional plane at the model mid-span. High spatial and temporal resolution has been achieved, and the flow on the upper side has been covered. For further details about the experimental set-up, the reader is referred to Le Pape *et al.*[8] and Heine *et al.*[6].

Two airfoil leading-edge configurations are available. The DVG leading edge can be exchanged with a smooth, clean leading edge. In the framework of the present study, this second configuration will be taken as non-controlled, or clean case reference.

2.1 Overall comparison between clean and controlled cases

2.1.1 Lift and moment comparison

The lift and moment cycles of the clean case show the classic dynamic stall characteristics (Fig. 2). During the upstroke phase of the cycle, the lift and moment are quasi-proportional to the AoA. When the maximal angle of attack (AoA) is reached and the airfoil begins the downstroke phase of the cycle, the lift plunges quickly as the pitching moment reaches large negative values. As the airfoil approaches the mean AoA, the lift is minimal and the negative pitching moment rises towards positive values. From the minimal AoA, the lift and moment recover their initial linear behavior.

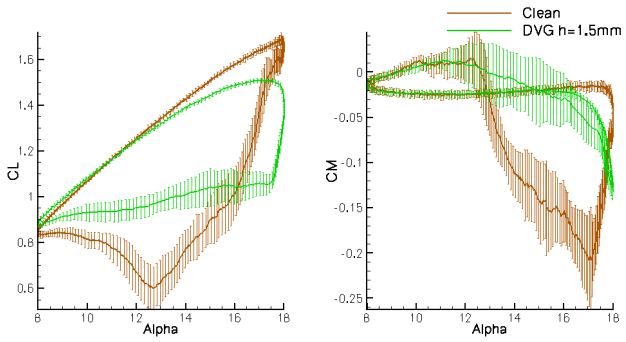

Figure 2: Lift (Left) and Moment (Right) coefficients compared between Clean and DVG-controlled cases. The coefficients are phase-averaged. The error bars are the standard deviation.

The effect of the DVG actuation is clearly visible in Fig. 2: the DVG reduces the minimal pitching moment peak by 36% at the cost of a maximal lift loss of 11% in the present flow conditions. The lift is much higher during the downstroke, and the hysteresis loop is much smaller. The DVG is very efficient at alleviating the main negative dynamic stall effect, i.e. the negative pitching moment, and the large lift loss during downstroke.

2.1.2 PIV velocity field comparison

The PIV velocity fields are used to identify the stalling behavior of the clean (Fig. 3) and DVG-controlled cases (Fig. 4). The presented PIV velocity fields have been phase-averaged over 18 images. Separation events are compared in the AoA range around the stall for the clean and controlled cases.

The clean case flow is fully attached during upstroke motion (Fig. 3(a)). When the rotational speed decelerates as the airfoil reaches the maximal angle of attack, the flow begins to separate at approximately 20% of the chord (Fig. 3(b)). At the maximal angle of attack, a sudden burst of recirculation (the Dynamic Stall Vortex or DSV) occurs from about 5-10% of the chord as the airfoil begins to move downstroke (Fig. 3(c)). Furher downstroke, the separation starts from the leading edge (Fig. 3(d)) and the airfoil is therefore completely separated. The flow is then progressively reattaching starting from the leading edge (Fig. 3(e)) and is fully reattached only shortly before reaching the minimal angle of attack (Fig. 3(f)).

The controlled case shows a trailing edge recirculation earlier than the clean case (Fig. 4(a)). The recirculation area is growing toward the leading-edge with increasing angle of attack (Fig. 4(b)). The separated region reaches a maximal extension starting at 25% chord at the highest angle of attack (Fig. 4(c)). The separated region then decreases progressively as the airfoil is moving downstroke (Fig. 4(d)). The flow is reattaching before reaching the mean angle of attack (Fig. 4(e)). No complete separation is observed in the PIV results: the first 25% of the airfoil are always attached during the oscillation cycle.

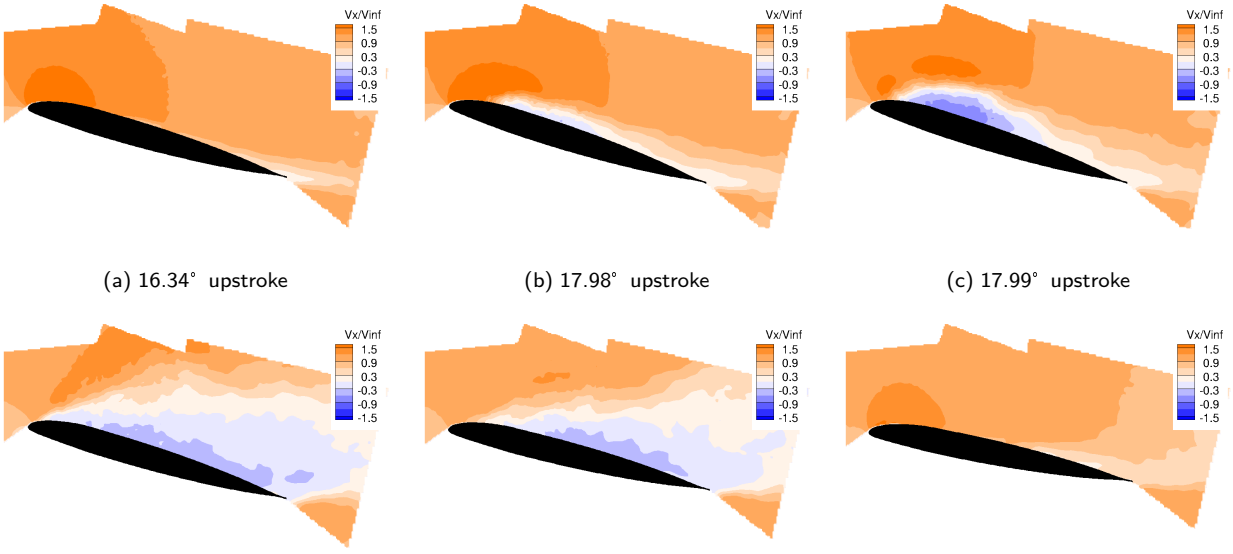

(a) 16.34° upstroke (b) 17.98° upstroke (c) 17.99° upstroke

(d) 16.92° downstroke (e) 14.34° downstroke (f) 11.85° downstroke

Figure 3: PIV V_x Velocity fields for different angles of attack in the stalling phase of the cycle of the clean airfoil.

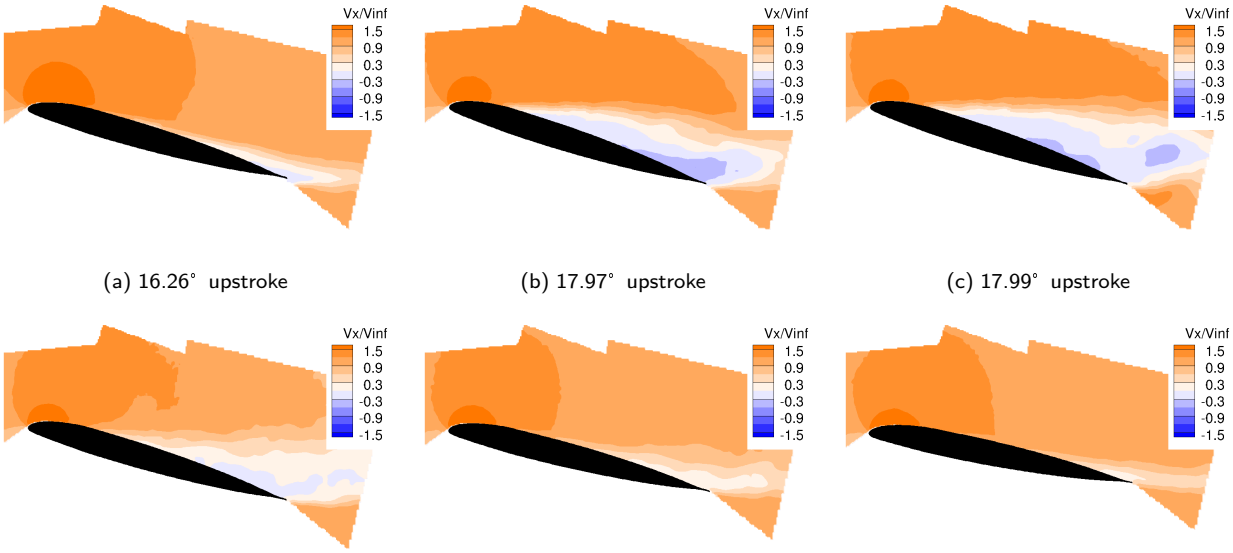

(a) 16.26° upstroke (b) 17.97° upstroke (c) 17.99° upstroke

(d) 16.98° downstroke (e) 14.44° downstroke (f) 11.96° downstroke

Figure 4: PIV V_x Velocity fields for different angles of attack in the stalling phase of the cycle of the DVG-controlled Airfoil.

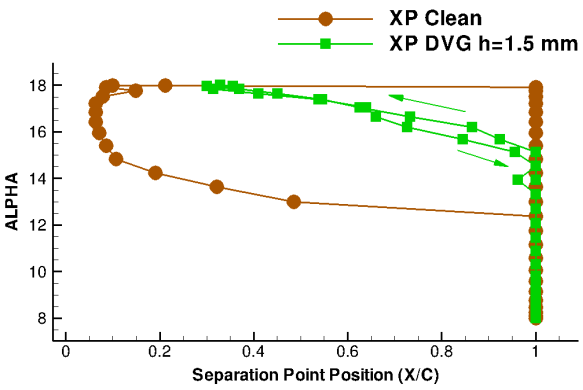

Figure 5: Comparison of the separation location motion over the airfoil upper surface between the clean and controlled cases. The separation location has been extracted from the phase-averaged PIV measurements.

An approximation of the separation location can be extracted from the phase-averaged PIV measurements, using as criterion the longitudinal velocity V_x sign change close to the airfoil surface (Fig. 5). Since the PIV does not provide any flow measurement in the near-wall region, the estimated separation is hereby located slightly downstream of the genuine separation point. The clean case stalling behavior is clearly of the "leading edge stall" type, while the controlled case switches to "trailing edge stall" type. This is in agreement with the static stall behavior observed for this DVG-controlled configuration by Le Pape *et al.*[8].

2.2 Understanding the DVG - induced control effect

In order to better understand the principle of operation of the DVG actuation, a Proper Orthogonal Decomposition (POD)[18] has been applied to the time-dependent PIV vector fields. With this method the detection of large-scale coherent structures is possible. The PIV vector fields are used to set an eigenvalue problem, which is solved to find a set of coefficients $a_i(t)$, eigenfunctions $\Phi_i(x)$ and eigenvalues λ_i for each eigenmode, which represents a fraction of the original flow field. Visualization of eigenfunction fields $\Phi_i(x)$ can help to identify physical flow phenomena for each mode. Comparison of the coefficient $a_i(t)$ over the time reveals the timing of the different modes.

In the present study the POD method is applied to all images obtained from PIV measurements. The resulting eigenmodes are then to be interpreted as follows [14],[6] : the first and second modes are the most present structures in a statistical sense, i.e. the fully attached (Fig. 6(a)) and separated flows (Fig. 6(b)). The third mode of the clean case (Fig. 6(c)) contains the strongest coherent structure beside the first two modes, and has been identified as the Dynamic Stall Vortex (DSV)[14]. Note that the third mode of the controlled case is completely different and cannot be interpreted as the same large coherent structure. One effect of the DVG control is to completely alleviate the dynamic stall vortex present in the clean case. From the fourth mode, the eigenfunctions are usually interpreted as weaker coherent structures, up to turbulence and eventually noise[6].

From the previous PIV velocity analysis, and from the observation of coefficients, the clean airfoil angle of attack range of stall can be discussed. The PIV in Fig. 3 shows clearly that stalling occurs as soon as the airfoil begins to move downstroke. The pitching moment remains negative until the AoA goes down to 12°, which is when the flow is fully reattached. Let us then define the stalled region from 18° to 12° downstroke. The visualization of the a_i coefficients shows the flow structures timing in Fig. 7.

The first coefficient a_1 is subjected to small variations over the oscillation cycle, because it represents the most present flow structure, i.e. the attached flow, in a statistical sense (Fig. 7(a)). For the clean case, the absolute value of a_1 diminish as soon as the stall AoA is reached, and remains low as long as the airfoil remains stalled. For the controlled case, the variation of a_1 occurs earlier, and the amplitude of variation is much smaller. This is in agreement with the previous PIV analysis which shows an earlier and smaller recirculation. The second coefficients a_2 of the clean and controlled cases (Fig. 7(b)) are rising when the airfoil is stalled. The coefficient of the controlled case starts growing earlier, which is to be correlated to trailing-edge recirculation. However, the third coefficients a_3 of the clean and controlled cases (Fig. 7(c)) are completely different. The clean case a_3 coefficient is close to zero outside stall. Since the third eigenmode is associated to the DSV for the clean case, this coefficient shows the bursting and dying of this specific structure within the flow.

Furthermore, the 4^{th} mode coefficient of the clean case is very similar to the 3^{rd} mode coefficient of the controlled case (Fig. 8(a)), and the 5^{th} mode coefficient of the clean case is very similar to the 4^{rd} mode coefficient of the controlled case (Fig. 8(b)). As recalled those higher eigenmodes are to be associated with weaker flow structures and turbulence. These smaller perturbations within the flow are created by the separation occurring both on the clean and controlled airfoil. Thus, the DVG might not qualitatively modify those modes, having only an effect on the third mode, i.e. the DSV.

3 Numerical simulations

The CFD method used is the ONERA multi - application aerodynamic code elsA [4], which solves the Euler-RANS equations for structured multi-block grids in finite-volume method. The space discretization scheme AUSM+(P) developed by Edward and Liou [3] is used for the inviscid fluxes. The numerical dissipation of this scheme is proportional to the local velocity, and thus remains low in the boundary layers. The viscous fluxes discretization use a classical cell-centered formulation. For unsteady RANS (URANS) computations, a second-order implicit time discretization method with

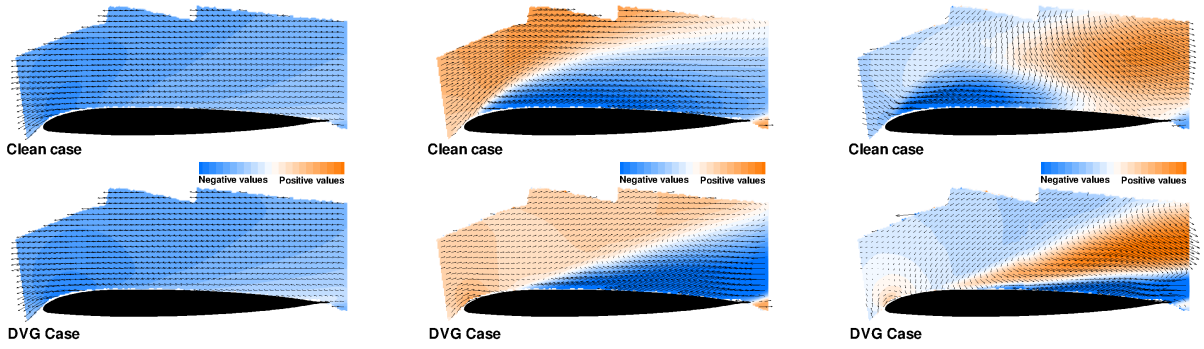

(a) $\Phi_1(x, y)$ (b) $\Phi_2(x, y)$ (c) $\Phi_3(x, y)$

Figure 6: First (a), second (b) and third (c) POD mode engenvectors fields for the clean and DVG-controlled cases. The field coloration correspond to the x-eigenvector eV_x. Note that these vector fields do not have direct physical meaning.

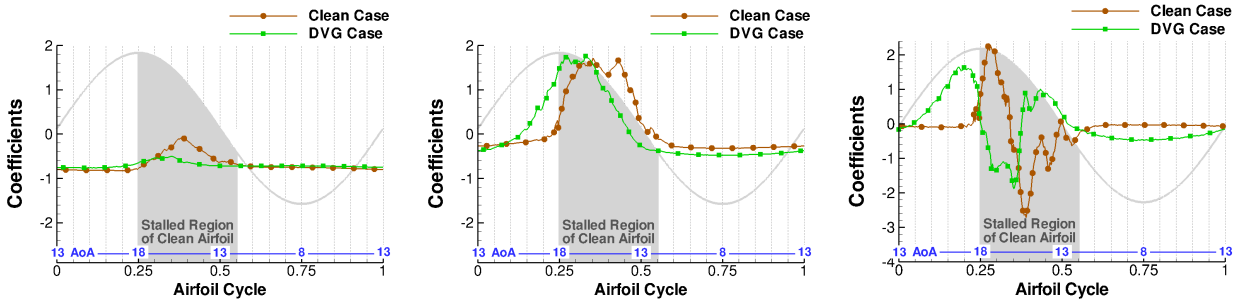

(a) First POD coefficient a_1 (b) Second POD coefficient a_2 (c) Third POD coefficient a_3

Figure 7: Comparison of the 1^{st} (a), 2^{nd} (b) and 3^{rd} (c) eigenmode coefficients for clean and controlled cases. The coefficients are undimensioned with the square root of the mode eigenvalue λ_i : $a_i/\sqrt{2\lambda_i}$. The grey curve represents the airfoil AoA over the time. The grey shaded area represents the clean airfoil stalled approximated region.

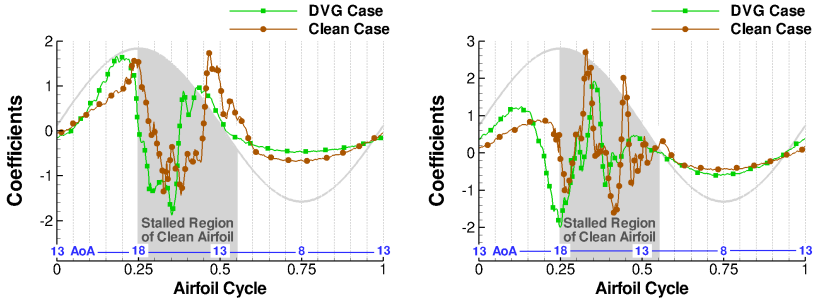

(a) (b)

Figure 8: Comparison of the 4^{th} mode coefficient of the clean case with the 3^{rd} mode coefficient of the controlled case (a); and 5^{th} clean case mode coefficient with the 4^{th} controlled case mode coefficient (b). See Fig. 7 for legend.

LU factorization and Newton iterations is applied. The two-equation $k-\omega$ turbulence model with Kok cross-derivative terms and SST correction [13] is used. External boundary conditions are non-reflecting type and are applied 20 chords away from the airfoil. Following previous results[15], the airfoil oscillation cycle has been divided in 18000 timesteps, which are computed over 25 Newton sub-iterations. The computations are considered converged as soon as the lift and moment evolutions are the same from cycle to cycle.

For clean (i.e. without stall control) calculations, a 2D C-shaped mesh is used. Its dimensions are 2141x209 for a 1900 nodes discretization around the airfoil. As shown previously[19] such a fine mesh is necessary in order to capture the laminar separation bubble in the leading-edge region of the airfoil. An laminar-transition criterium is applied as in reference [15]. Four cycles are computed in order to reach the convergence.

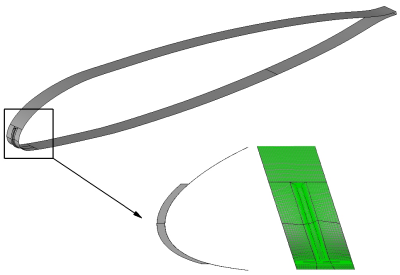

Figure 9: Airfoil and DVG geometry as used for numerical simulations.

For controlled (i.e. with DVG) calculations, a 3D mesh including the complete DVG geometry is used (Fig. 9). The aifoil 3D C-shapes basis grid is 501x121x37 large, with 300 nodes around the airfoil. The mesh span is as large as the DVG spanwise spacing (2.3 % of the chord). The spanwise discretization was proved to be an acceptable compromise between computational cost and mesh convergence. Periodic boundary conditions are applied in the spanwise direction. From previous work on static stall control using the same configuration, the laminar-turbulent transition is presumed to happen at the very most upstream zone of the DVG [7]. Thus, the flow is supposed fully turbulent and the laminar-turbulent transition is not taken into account. Three cycles are necessary in this case to reach the convergence.

The RANS equations solution corresponds to the steady simulation of the mean flow. As the unsteady extension of the RANS method, URANS is therefore only able to simulate the mean flow temporal motion. Thus, the overall URANS does not provide a mean flow in a statistical sense, being related to the time-dependent mean flow within the sub-iterations only. Therefore, time-dependent numerical solutions have to be considered as instantaneous snapshots of the flow. In order to qualitatively compare the simulations and the experiment, instantaneous PIV results are adapted.

3.1 Overall comparison between experimental data and numerical simulations

The numerical simulation of dynamic stall is an old and not yet resolved problem[15]. For 2D simulation of the clean case, good agreement in the upstroke part of the cycle as well as the large discrepancies in the downstroke part in Fig. 10(a) are not unexpected. The overall lift and moment min-max amplitude are overestimated of about 100%, with a large lift peak at the beginning of the downstroke motion and a very deep lift and moment loss in the downstroke part of the cycle. However, this computation represents the best achievable result using the current 2D URANS methods.

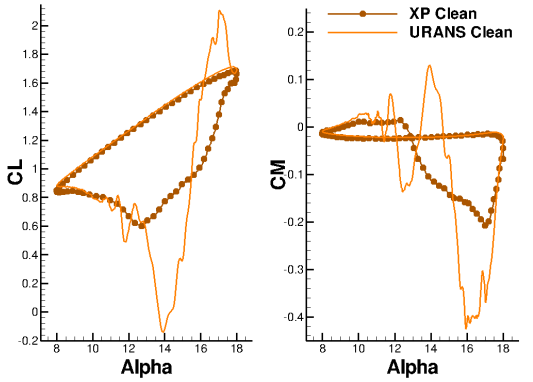

(a) Clean case.

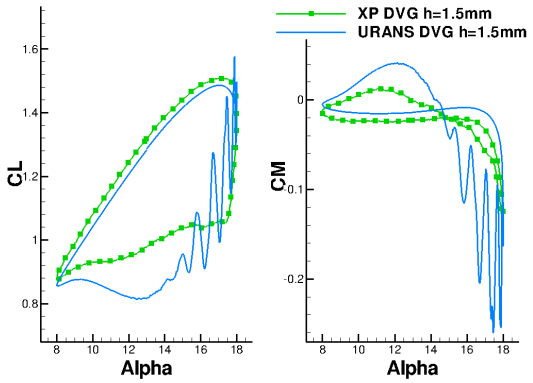

(b) DVG case.

Figure 10: Lift and moment comparisons between experimental references and computations for the clean (a) and DVG-controlled (b) cases.

DVG computational lift and moment coefficients are in fair agreement with the experimental reference in the upstroke phase (Fig. 10(b)). However, as soon as the airfoil is moving downstroke the computation shows discrepancies. The maximal pitching moment is overestimated by 50% and strong oscillations of the lift and moment coefficients are observed. The oscillation frequency can be estimated at $87Hz$, and can be linked to the vortical structures occurring in the flow (s. part 3.2.2). Nevertheless, the gain in pitching moment between the clean and DVG simulations is about 39%, which is very close to the 36% observed

between experimental clean and DVG cases. Thus, the overall control effect is indeed fairly reproduced in the numerical simulation.

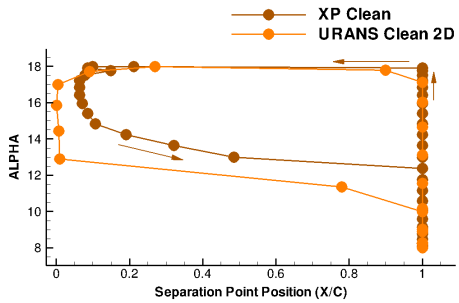

(a) Clean case.

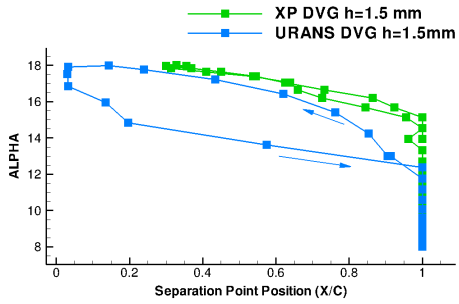

(b) DVG case.

Figure 11: Comparisons with respect to the experimental data of the estimated separation location for the clean (a) and DVG-controlled (b) cases.

From wall friction values extracted from the numerical flow solutions, it is also possible to estimate the separation point motion during the airfoil cycle (Fig. 11). The clean case numerical solution is in fair agreement with the experimental reference, showing indeed the same leading-edge stall behavior. The DVG computation shows qualitatively the correct trailing-edge stall behavior, but has a larger recirculation zone. Hence, the separation point is located at 3% of the chord instead of the 25%. However, since the separation point detection methods are different for experimental and numerical cases, this comparison has to be be interpreted cautiously.

3.2 Comparison with time-resolved PIV data

In order to characterize the discrepancies between measured flow and simulations, the PIV instantaneous field are used as references.

3.2.1 Clean case

As stated from the lift and moment analysis, the computation is in very good agreement as long as the flow is attached (Fig. 12(a)). At the beginning of the downstroke phase, the computed flow is still attached and no separation occurs (Fig. 12(b)). The simulation shows a massive separation much later only at the moment peak AoA (Fig. 12(c)). Finally, the reattachment occurs at almost the same moment in the simulation and experiment.

The onset of the dynamic stall obviously happens in computation and experiment at different times. From the observation of the stall onset (Fig. 13) several statements can be made. The generated vortical structures are very similar between experiment and numerical simulation (Fig. 13(b)). The dynamic stall vortex (DSV) is clearly visible. However, note that DSV structure evolves in a different way between the computation and the experiment. The numerical DSV remains strong and coherent while the PIV shows an cloud of small scattered vortices whose effect on the airfoil surface pressure is limited (Fig. 14). The downstream advection of those strong vortices in the simulation explains the large lift and moment amplitude oscillations.

3.2.2 DVG-controlled case

The DVG-controlled computations are compared to PIV data in Fig. 15. The simulation is in overall good agreement with the experimental reference. Separation occurs during the upstroke part of the cycle at almost the same time in both computed and measured flows (Fig. 15(a)), which is in agreement with the previous lift and moment coefficients comparison. Furthermore, the separated zone size is very similar between computation and PIV during the downstroke phase of the cycle (Fig. 15(c)).

Vorticity can bring further information with regard to the coherent structures occurring in the flow (Fig. 16). In the PIV, the flow is characterized by a clockwise rotating vorticity generated by the leading edge, and an anti-clockwise rotating vorticity generated by the trailing edge of the airfoil. This general behavior is fairly reproduced in the numerical simulation. However, the vorticity field contains numerous small vortices in the PIV. Differently, the URANS computation produces strong vortices or vorticity spots, where vorticity is much more concentrated. As a consequence, strong coherent vortices are shed downstream of the airfoil. From two numerical solutions taken at slightly different timesteps (Fig. 16), the estimated frequency of this vortex shedding is $87Hz$. This was the lift and moment oscillation frequency previously mentioned.

Furthermore, the vorticity field images suggest a separation height of about 3 times the airfoil thickness above the airfoil the trailing edge. Using this lenght, the theoretical shedding frequency for a Strouhal number of 0.2 would approximately be $81Hz$, which is very close to the observed frequency.

Similarities in both clean and controlled numerical simulations suggest a common weakness in the computational methodology. The presence of strong oscillations on the lift and moment diagram during the downstroke phase is indeed to be linked to the strong vortex shedding occurring downstream of the separated

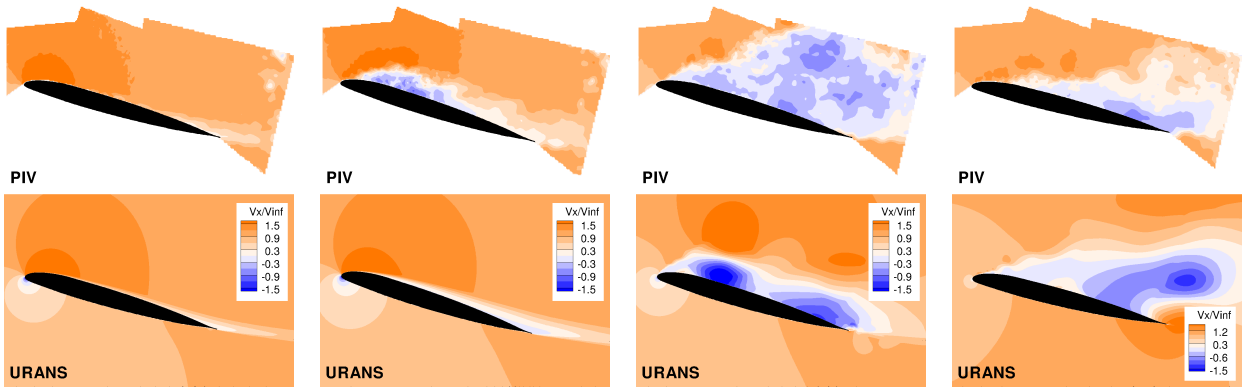

(a) 16.34°upstroke. (b) 17.99°upstroke. (c) 16.42°downstroke. (d) 14.34°downstroke.

Figure 12: V_x instantaneous PIV fields compared to URANS numerical simulations at different AoA for the clean case.

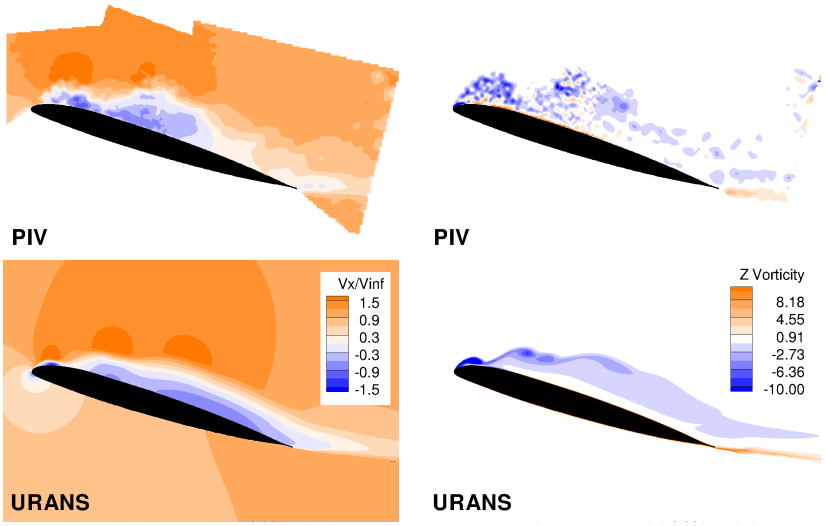

(a) Velocity. (b) Vorticity.

Figure 13: V_x (a) and Vorticity (b) instantaneous PIV fields *vs.* URANS numerical simulations for the clean case at slightly different AoA. PIV: 17.96°, URANS: 17.43° downstroke.

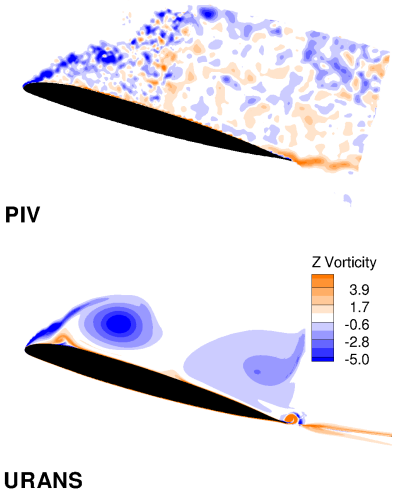

Figure 14: Vorticity instantaneous PIV field at the moment peak compared to URANS numerical simulations for the clean case at 16.42° downstroke.

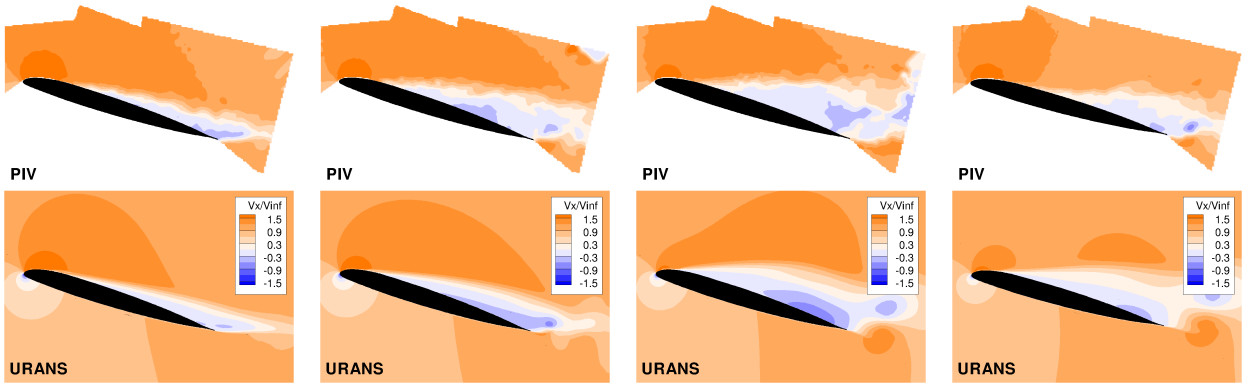

(a) 17.75°upstroke. (b) 17.99°upstroke. (c) 17.52°downstroke. (d) 15.92°downstroke.

Figure 15: V_x instantaneous PIV fields compared to URANS numerical simulations at different AoA for the controlled case.

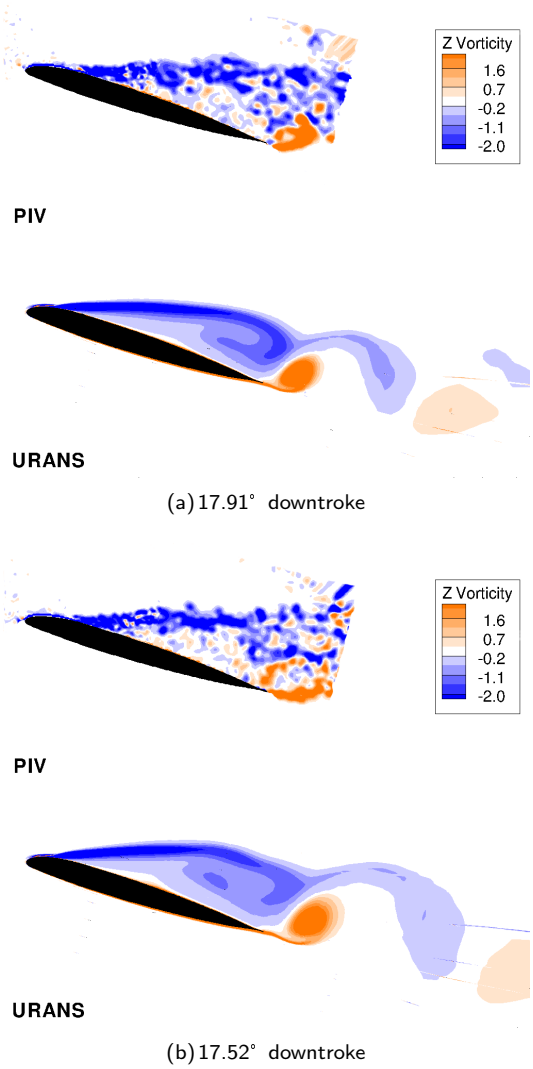

Figure 16: Vorticity field at 17.91° (a) and 17.52° downstroke (b) for instantaneous PIV and URANS numerical simulations of the DVG-controlled case.

flow region. This vortex shedding is different from the PIV measurements, where only smaller vortices are observed. The mentioned oscillations are then to be associated with the flow modeling of the numerical simulations. Since the massive separation behind a bluff body is clearly 3D[16], the chosen grids for dynamic stall computations are to be questioned. Influence of the span grid extension for massive separation simulation has been the subject of several studies. Breuer *et al.*[1] demonstrate that a span size equal to the airfoil chord is at least necessary. Shur *et al.*[17] conclude that span grid length has a large influence on computed flow separation. This suggests that a too narrow computational grid (2D for the clean case, or 3D with only 2.3% of the chord as span size for the DVG) seems to be the main reason of such effect. This inability for the coherent structures to develop spanwise could explain the presence of too strong vortices in the numerical simulations.

3.3 Analysis of the vortex generation

The flow topology around the DVG geometry can be described as shown in Fig. 17 : several vortices are observed; the main positive vortex is generated from the downstream edge of the DVG and merges with a second positive vortex coming from the upstream edge of the DVG. Secondary negative vortices are interacting with the previous positive vortices. This flow topology is the same as it was in our previous DVG-controlled static stall study. From cut planes normal to the airfoil surface(Fig. 18(a)), the circulation of the main positive vortex can be estimated by integrating the vorticity. The circulation decay over the first 25% of the chord is the same for different AoA (Fig. 18(b)). From the leading edge, a strong decrease of the vortex strength occurs first due to vortices interactions. Further downstream the circulation decreases then more gently because of the natural and numerical dissipation. This behavior is similar to the one observed in the previous static stall control study.

From our previous work conclusions in [7], the DVG effect can be described. Through the helical motion

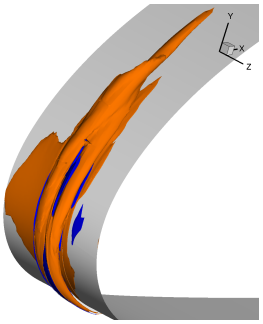

(a) Helicity isosurfaces.

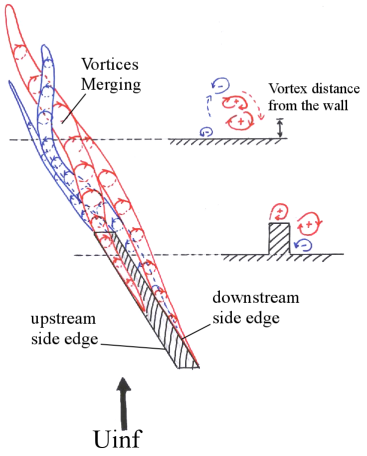

(b) DVG Vortex generation scheme.

Figure 17: Helicity isosurfaces at 17.91° (a). Scheme of the vortices generation around the DVG geometry (b). Figure taken from [7].

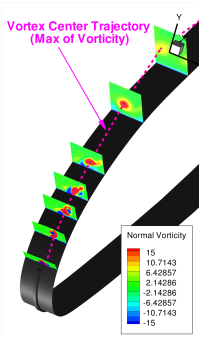

(a) Vorticity planes for circulation estimation.

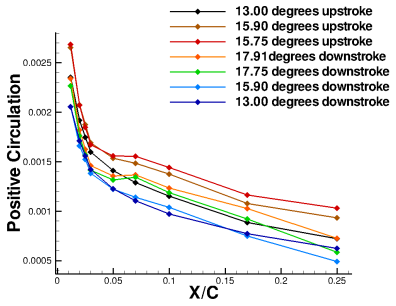

(b) Circulation *vs* position along the airfoil.

Figure 18: Circulation estimation method (a), and circulation of the main generated vortex along the airfoil for different AoA (b).

induced by the generated vortices, the DVG adds energy to the boundary layer. This makes the leading-edge boundary layer less receptive to the adverse pressure gradient. The generated vortex also produces local separations and perturbations. As consequence the boundary layer at the trailing edge has less energy and separates earlier. The overall stall behavior is therefore modified from leading edge to trailing edge type. Since the leading edge is always attached thanks to the DVG-generated vortices, the DSV cannot develop as in the clean case and is not observed in the previous PIV and POD analysis.

4 Conclusion and perspectives

In the current paper, our investigations and results in the research scope of the OA209 airfoil dynamic stall control using a leading-edge deployable vortex generator (DVG) are described. The present study focuses on the DVG control effect by means of experimental data and URANS computations analysis.

The experimental pressure measurements give access to general comparison of lift and moment coefficients between the clean case and DVG-controlled case. Through PIV post-processing the separation point motion is compared between the clean case and DVG-controlled case. The DVG modifies the airfoil stall behavior from leading-edge to trailing-edge type. From Proper Orthogonal Decomposition, the DVG effect on the flow separation is highlighted, showing a complete alleviation of the third POD eigenmode i.e. the dynamic stall vortex, and not modifying the higher eigenmodes.

The URANS numerical simulations of the clean and DVG-controlled configurations are compared with experimental data. Both simulations show good agreement with experiments as long as the airfoil is moving upstroke. Discrepancies are found in the downstroke phase of the cycle. However, these discrepancies are a numerical effect, which is believed to be a consequence of the computational grid span size. The clean case computation stall onset and the DVG separation are qualitatively correctly simulated. The DVG control effect between clean and controlled cases is fairly reproduced in the computations.

Finally, the DVG vortex topology and circulation study brings a better understanding of the DVG-induced control. The DVG-induced vortex strength is evaluated and is shown to behave similarly to static stall control case. Because of the DVG, the leading-edge is always attached and the Dynamic Stall Vortex cannot appear.

This work raises several questions about the numerical methodology used for dynamic stall clean and controlled configurations. A span size study would give answers to the possible grid effect on the dynamic stall control simulation. In order to refine the comparison with experimental data, a POD analysis of the time-resolved computed solution may prove useful. Finally,

an application of the numerical simulation and PIV comparison to other dynamic stall cases may provide further understanding of the DVG control effect.

Acknowledgements

This work has been part of the ONERA and DLR joint project "Advanced Simulation and Control of Dynamic Stall"(SIMCOS). The authors also gratefully acknowledge the whole F2 wind-tunnel team, as well as Karen Mulleners from the DLR Helicopter Department and Michel Costes from the ONERA Applied Aerodynamics Department.

References

[1] M. Breuer and N. Jovicic. Separated flow around a flat plate at high incidence : an LES investigation. *Journal of Turbulence*, 2001.

[2] M. Chandrasekhara, M.C. Wilder, and L.W. Carr. Unsteady stall control using dynamically deforming airfoils. *AIAA Journal*, 1997.

[3] J. R. Edward and M. S. Liou. Low diffusion flux-splitting methods for flows at all speeds. *AIAA Journal*, 36:1610–1617, 1998.

[4] M. Gazaix, A. Jolles, and M. Lazareff. The elsA object-oriented computational tool for industrial application. In *23 ICAS conference*, September 2002.

[5] V. Gleize, M. Costes, A. Le Pape, and F. Richez. Numerical simulation of a pitching airfoil under dynamic stall conditions including laminar/turbulent transitions. In *46th AIAA Aerospace Science Meeting, RENO, USA*, January 2005.

[6] B. Heine, K. Mulleners, G. Joubert, and M. Raffel. Dynamic stall control by passive disturbance generator. In *41th AIAA Fluid Dynamics Conference and Exhibit, Honolulu, Hawaii*, 2011.

[7] G. Joubert, A. Le Pape, and S. Huberson. Numerical study of flow separation control over a OA209 airfoil using deployable vortex generator. In *49th AIAA Aerospace Sciences Meeting AIAA-2011-1044*, 2011.

[8] A. Le Pape, M. Costes, F. Richez, F. David, and J.M. Deluc. Experimental study of dynamic stall control using deployable leading-edge vortex generator. In *American Helicopter Society 67th Annual Forum*, 2011.

[9] H. Mai, G. Dietz, W. Geissler, K. Richter, J. Bosbach, H. Richard, and K. DeGroot. Dynamic stall control by leading edge vortex generators. In *American Helicopter Society, 62nd Annual Forum (Phoenix, AZ)*, 2006.

[10] Preston Martin, John Berry, Tin-Chee Wong, Marvin Moulton, and Michael McVeigh. Passive control of compressible dynamic stall. 2008.

[11] K. W. McAlister and C. Tung. Suppression of dynamic stall with a leading-edge slat on a vr-7 airfoil. Technical report, NASA, 1993.

[12] W. J. McCroskey and R. K. Fisher. Dynamic stall of airfoils and helicopter rotors. *AGARD R 595*, pages 2.1 – 2.7, 1972.

[13] Menter. Zonal two-equations k-omega turbulence model for aerodynamic flows. *AIAA Journal*, 1993.

[14] Karen Mulleners. *On the Coherent Structures behind the Phenomenon of Dynamic Stall*. PhD thesis, Deutsches Zentrum fr Luft- und Raumfahrt - Intitut für Aerodynamic und Strömungstechnik Göttingen, 2010.

[15] K. Richter, A. Le Pape, T. Knopp, M. Costes, V. Gleize, and A.D. Gardner. Improved two-dimensional dynamic stall prediction with structured and hybrid numerical methods. In *American Helicopter Society, 65th Annual Forum*, 2009.

[16] Gnter Schewe. Reynolds-number effect in flow around more-or-less bluff bodies. *Journal of Wind Engineering and Industrial Aerodynamics*, 89:1267–1289, 2001.

[17] M. Shur, P.R. Spalart, K.D. Squire, M. Strelets, and A. Travin. Three Dimensionality in Reynolds-Averaged Navier-Stokes solutions around two-dimensional geometries. *AIAA Journal*, 43:1230–1242, 2005.

[18] L. Sirovitch. Turbulence and the dynamic of coherent structures, part i, ii and iii. *Q. Appl. Math.*, 45(3):561–590, October 1987.

[19] J. Szydlowski and M. Costes. Simulations of flow around a static and oscillating in pitch NACA 0015 airfoil using URANS and DES. In *ASME Heat Transfer/Fluids Engineering Summer Conference*, 2004.

[20] J.J. Thibert and J. Gallot. Advanced research on helicopter blade airfoils. *Vertica*, 5:279–300, 1981.